

Geophysical Imaging of Stimulated Microbial Biomineralization

KENNETH H. WILLIAMS,^{*,†,‡}
 DIMITRIOS NTARLAGIANNIS,[§]
 LEE D. SLATER,[§] ALICE DOHNALKOVA,^{||}
 SUSAN S. HUBBARD,[‡] AND
 JILLIAN F. BANFIELD^{†,‡}

Department of Environmental Science, Policy, and Management, University of California, Berkeley, California 94720, Lawrence Berkeley National Laboratory, Berkeley, California 94720, Department of Earth and Environmental Sciences, Rutgers University, Newark, New Jersey 07102, and Pacific Northwest National Laboratory, Richland, Washington 99352

Understanding how microorganisms influence the physical and chemical properties of the subsurface is hindered by our inability to observe microbial dynamics in real time and with high spatial resolution. Here, we investigate the use of noninvasive geophysical methods to monitor biomineralization at the laboratory scale during stimulated sulfate reduction under dynamic flow conditions. Alterations in sediment characteristics resulting from microbe-mediated sulfide mineral precipitation were concomitant with changes in complex resistivity and acoustic wave propagation signatures. The sequestration of zinc and iron in insoluble sulfides led to alterations in the ability of the pore fluid to conduct electrical charge and of the saturated sediments to dissipate acoustic energy. These changes resulted directly from the nucleation, growth, and development of nanoparticulate precipitates along grain surfaces and within the pore space. Scanning and transmission electron microscopy (SEM and TEM) confirmed the sulfides to be associated with cell surfaces, with precipitates ranging from aggregates of individual 3–5 nm nanocrystals to larger assemblages of up to 10–20 μm in diameter. Anomalies in the geophysical data reflected the distribution of mineral precipitates and biomass over space and time, with temporal variations in the signals corresponding to changes in the aggregation state of the nanocrystalline sulfides. These results suggest the potential for using geophysical techniques to image certain subsurface biogeochemical processes, such as those accompanying the bioremediation of metal-contaminated aquifers.

Introduction

The problem of groundwater contamination by acid-mine drainage, industrial sources, and government nuclear weapons programs has spawned interest in the ability of microorganisms to facilitate remediation through sequestration of metals in insoluble precipitates (1–4). One major barrier

to successful implementation of bioremediation has been the inability to monitor microbial activity and mineral precipitation at sufficiently high spatial resolution and over large enough areas to understand where, when, and how treatment is occurring (5, 6). In addition, although biostimulation may prove initially effective, it may be difficult to verify stability of the treatment in the long term (7). Here, we demonstrate a method analogous to noninvasive medical imaging techniques that enables time-resolved imaging of dynamic subsurface processes. Development of such techniques at the field scale could be invaluable for guiding environmental remediation approaches and for monitoring long-term stewardship activities at contaminated sites.

High-resolution geophysical techniques have proven extremely useful at the field scale for estimating hydrogeological properties (e.g., lithology, hydraulic conductivity, and moisture content), providing information about subsurface environments not directly accessed by boreholes (8). Although numerous studies have utilized such techniques to detect abiotic changes in physical and chemical properties (9–11), relatively few have explored their use in monitoring microbial processes in the subsurface (12, 13). In this study, we test the sensitivity of two geophysical techniques, complex resistivity and acoustic wave propagation, to the products of microbial biomineralization.

All active geophysical techniques are based upon the principle of introducing a source signal (e.g., an electrical current or an acoustic wave) into a volume of subsurface material and measuring the resulting response signal at selected locations (either at the surface or in boreholes) within this volume. Subtle changes in the physical and chemical properties of the material can dramatically alter the response signals. Such property differences include changes in fluid and rock conductivity, grain size, consolidation state, and degree and type of pore fluid saturation (14). The geophysical techniques studied here are impacted to varying degrees by such changes, in particular, those affecting the electric charge carrying capacity (complex resistivity) and the elastic moduli of sediments and pore fluids (acoustic wave propagation).

For subsurface investigations, the complex resistivity method involves the injection of variable frequency currents into the ground and the measurement of resulting voltage potentials via electrodes located both above and below the ground surface. Differences between phase and magnitude of the measured potentials relative to the injected current determine the frequency-dependent electrical resistivity of the subsurface. Regions exhibiting a strong frequency dependence (i.e., those exhibiting a large phase shift) are found to correspond to areas where charge migration by electrolytic transfer in the pore fluid is impeded due to a variety of interfacial conduction mechanisms (15). These include regions where the charge transfer changes from electrolytic to electronic (such as in pore-blocking mineralized rocks) or where grain surface features impede the normal flow of current carrying ions (such as in clay-bearing zones or other areas of high surface charge density). As a result, reactions that alter the way in which electric charge is conducted through the pore space (e.g., mineral precipitation) should lead to observable changes in the measured phase response of sediments undergoing bioremediation.

The acoustic wave technique relies on the propagation of acoustic or mechanical waves through the subsurface. Changes in both velocity and amplitude of the waves are directly related to the bulk elastic properties of the sediments and pore fluids, which in turn depend on compositional

* Corresponding author e-mail: khwilliams@lbl.gov; phone: (510)-701-1089.

[†] University of California, Berkeley.

[‡] Lawrence Berkeley National Laboratory.

[§] Rutgers University.

^{||} Pacific Northwest National Laboratory.

variations in rock type, fluid chemistry, and intergranular structure (16). Recent advances in modeling acoustic wave propagation have shown mixed porosity systems to be of critical importance in governing the degree to which wave amplitudes are attenuated (17). These models predict that local environments having heterogeneous pore-scale properties can represent regions of significant acoustic wave attenuation. As a result, reactions leading to the creation of subsurface heterogeneity (e.g., areas of mineral precipitation/dissolution, biomass development, etc.) may alter the way in which acoustic waves pass through regions undergoing enhanced metabolic activity.

Our primary objective was to follow the reaction dynamics of a column-scale biostimulation experiment using conventional biogeochemical and mineralogical measurements, as well as using noninvasive geophysical techniques. We tested the hypothesis that metal sequestration via microbe-induced sulfide precipitation creates physical property changes that directly alter the response of geophysical signals. We compared the temporal response of such signals against concomitant changes in fluid chemistry and microbial biomass to investigate if the geophysical responses are sensitive to the products of biomineralization. Finally, we validate our interpretation of the geophysical responses using electron microscopy techniques.

Materials and Methods

We investigated the use of geophysical techniques for monitoring microbe-induced ZnS and FeS precipitation within saturated sand-packed columns using the sulfate-reducing bacterium *Desulfovibrio vulgaris*. The experiments were conducted under temperature-controlled conditions over a period of 78 days using five polycarbonate columns having inner diameters of 5.0 cm and lengths of 30.5 cm (see Supporting Information). Each column was designated for a specific set of measurements, including multi-port fluid sampling, complex resistivity, acoustic wave propagation, and two abiotic controls. The control columns differed only in their lack of inoculum and were used to test abiotic geochemical effects on the geophysical signals. Fluid samples and geophysical data were collected every 3–6 days along the length of the column, with more frequent sampling earlier in the experiment. Upon termination, the three inoculated columns were destructively evaluated, and sediment samples were collected to determine grain-affixed biomass, extractable metals, and provide material for electron microscopy.

The sand used to fill the columns was composed of 99.8% quartz and 0.2% magnetite with particle diameters ranging from 600 to 800 μm . The sand was pretreated with H_2O_2 and a mixture of sodium citrate, NaHCO_3 , and $\text{Na}_2\text{S}_2\text{O}_4$ to remove organics and iron oxides before being rinsed, autoclaved, and dried at 105 °C. The columns were sterilized using ethylene oxide, and the sand was added in a way that minimized grain sorting through gentle tapping of the column. The porosity of the sand varied slightly for each column and was determined to be 0.37 ± 0.01 , with a resulting pore volume being 229 mL (± 6 mL). To eliminate entrapped air bubbles, each column was flushed with sterile N_2 before being saturated with 10 pore volumes of deaired and autoclaved, lactate-deficient feed solution.

The feed solution used to saturate the columns had previously been found to support growth of *D. vulgaris* and was designed to resemble metal- and sulfate-rich groundwater amended with a source of organic carbon (lactate). Final molar concentrations of the primary constituents were as follows: lactate, 2.8 mM; SO_4^{2-} , 3.93 mM; Zn^{2+} , 306 μM ; and Fe^{2+} , 360 μM . The fluid conductivity of the influent solution was $1300 \pm 40 \mu\text{S}/\text{cm}$ and remained stable over the experimental period. The fluids were rendered anoxic by boiling and cooling under a stream of N_2 and were heat

sterilized at 121 °C for 15 min. Before being introduced to the columns, the redox potential of the solution was lowered to an E_h value characteristic of sulfate reduction (-100 mV) through the addition of a mixture of sodium thioglycollate and ascorbic acid (18).

Cells of *D. vulgaris* were grown to stationary phase in an enriched (10X) version of the feed solution, centrifuged, rinsed three times, and resuspended in a lactate-deficient version, 20 mL of which was injected into each column via a syringe needle inserted 13–16 cm below the top. Standard methods for the culture of anaerobic bacteria were used throughout. The cells were allowed to affix to the sand grains for a total of 4 days before commencing flow, after which time lactate-amended fluids were introduced to each column from the bottom using a multichannel peristaltic pump. The columns were operated under continuous advective flow at a rate of 1.75 pore volumes per day, equivalent to a pore water velocity of 0.53 m day^{-1} . All experiments were conducted within an anaerobic chamber maintained under an atmosphere of N_2/H_2 (95:5).

Solution samples from the influent, effluent, and multi-port samplers (located at 3.8 cm intervals) were analyzed for major dissolved components at 3–5 day intervals over the first month of the experiment and with less frequency thereafter. Total dissolved Zn and Fe was determined by inductively coupled plasma atomic emission spectroscopy (ICP-AES). Lactate, acetate, and sulfate concentrations were determined by gradient elution ion chromatography (IC). Solution pH was measured using a sulfide-tolerant electrode. Planktonic cell concentrations were determined using quantitative live/dead staining (19) for each sampling location at six time points during the experiment (days 2, 12, 19, 29, 53, and 64).

Electrical measurements of both phase (ϕ) and conductivity magnitude ($|\sigma|$) were made with a two channel dynamic signal analyzer operated over the frequency range of 0.1–1000 Hz (20). Eight nonpolarizing Ag/AgCl electrodes were placed 3.5 cm apart along the length of the column, with inert gold current injection electrodes placed at either end. To minimize spurious polarization effects, the electrodes did not lie within the current flow path but were instead electrically coupled through the walls of the columns via a gel-based electrolyte that was found not to impact the quality of the measurements. Measurements were made between pairs of electrodes for all possible locations approximately once per week, with a more frequent interval earlier in the experiment.

Acoustic wave measurements were made using two fluid-coupled 1000 kHz piezoelectric transducers connected to a high-voltage pulser-receiver. An acoustic wave pulse was emitted from the source transducer and detected by the receiving transducer located on the opposite side of the column. The transducers were maintained in a fixed position within the walls of a fluid-filled tube into which the column was placed; it was then raised and lowered to make measurements along the length of the inoculated and control columns. Velocity and amplitude were determined for each location using the arrival time of the first break and the maximum peak-to-peak voltage, respectively, and compared to the corresponding baseline values. Measurements were made in 2 cm increments approximately once per week, with a more frequent interval earlier in the experiment.

Saturated hydraulic conductivity (K_s) measurements were obtained for both an inoculated and a control column at four times (baseline and days 17, 20, and 53) during the experiment using a constant head gradient method. Fluid flow was established for a specific head differential (7.0 cm), and the volume of fluid passing through the column per unit time was determined.

Following the 78 day flow period, destructive analysis provided samples for determining the concentration of sediment-affixed metal sulfides and microbial biomass. The distribution and concentration of solid-phase Zn and Fe on the sand grains was determined by extraction of 1.0 g samples in 5 M HCl (collected at 2 cm intervals from each of the three inoculated columns). The dissolved solution was filtered, diluted with deionized water, and analyzed by ICP-AES for total Fe and Zn. The grain-affixed biomass was determined through phospholipid fatty acid analysis of 5.0 g samples (collected at 3.5 cm intervals from each of the three inoculated columns) using methods described elsewhere; the total extractable polar lipids were used to determine the viable biomass per gram of sediment for each location (21).

Post-experimental analysis also provided samples for characterizing microbe–mineral associations and the crystal size and aggregation state through the use of scanning and transmission electron microscopy. Samples for SEM were collected at 4.0 cm intervals along each of the columns in a method similar to that of Vandevivere and Baveye (22). These were immersed overnight in a 2.5% solution of glutaraldehyde, rinsed 3 times in phosphate buffer, dehydrated in an ethanol series, and dried in a critical point drying unit with CO₂ as the transitional fluid. Samples were extruded onto carbon-coated stubs, sputter-coated with carbon, and analyzed using a Philips XL30 SEM fitted with backscattered and secondary electron detectors. Solid phases were prepared for TEM analysis by immersing 0.5 g of sediment in 2.5% glutaraldehyde and gently shaking to separate the cells and precipitates from the sand grains. The supernatant was removed and allowed to fix overnight, before being rinsed in phosphate buffer, dehydrated in an ethanol series, and embedded in LR White hard grade resin. The polymerized samples were sectioned on a microtome (70 nm thickness) and analyzed using a JEOL 2010 TEM operating at 200 kV. All SEM and TEM samples were preserved anaerobically until the time of analysis.

Results

Aqueous Phase Dynamics. The influent solution concentrations of lactate, SO₄^{2−}, Zn, and Fe for all columns remained relatively constant over time, with variations never exceeding ±1–2% of their initial values. In contrast, concentrations of these same species near the point of inoculation (19.0 cm from the inlet) began to decrease following a 3–4 day lag period, reflecting a delay in the onset of sulfate reduction (Figure 1A). Lactate concentrations fell from influent values of 2.8 mM to levels below detection after 10 days. With the exception of a 4–5 day period, they remained depleted for the duration of the experiment. Sulfate concentrations decreased from influent values of ~3.9 mM to concentrations of ~2.3 mM by day 10, before declining to pseudo-steady-state concentrations of 1.6 mM by day 30. This represents a total decrease in sulfate of 2.4 mM, yielding a consumption rate of 0.93 mmol kg^{−1} day^{−1}. Acetate concentrations inversely tracked those of lactate and sulfate, increasing from levels below detection to a maximum concentration of 2.3 mM by day 50. Aqueous Zn and Fe concentrations decreased from their influent values (0.31 and 0.36 mM, respectively) to levels essentially below detection by day 12 in a pattern closely following that of sulfate. Dark-colored mineral precipitates were visible in each of the inoculated columns following the onset of decreasing sulfate and metal concentrations. Variations in the effluent pH were modest over the experimental period, never varying by more than ±0.3 units from their influent value of 6.8. The influent fluids were compositionally identical for both inoculated and abiotic control columns, and no significant change in the effluent concentrations of lactate, sulfate, Zn, or Fe was observed for the control column (data not shown).

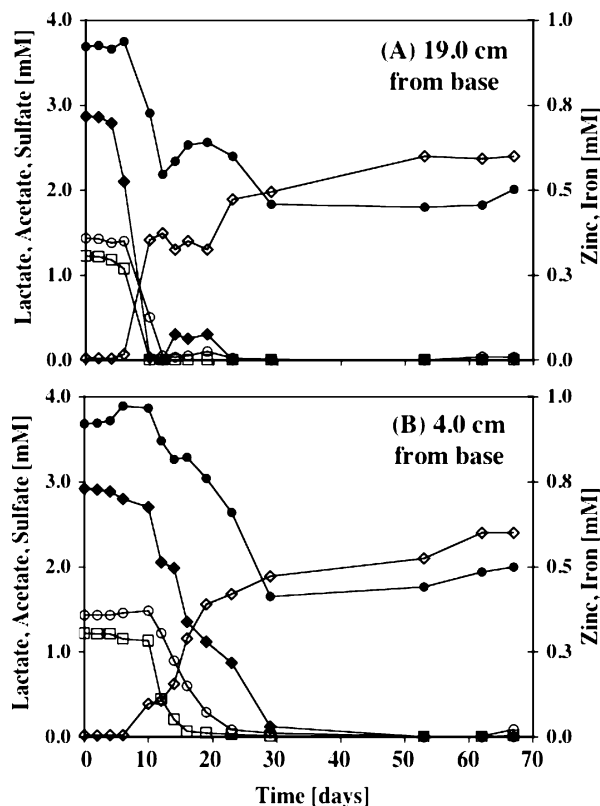


FIGURE 1. Inoculated column solution chemistry during the stimulation of *D. vulgaris* in the presence of aqueous zinc and iron: lactate (◆), acetate (◇), sulfate (●), Fe (○), and Zn (□). Metal concentrations are plotted on the right-hand axes. Data from two locations are shown, with (A) 19.0 cm and (B) 4.0 cm from the column base, respectively.

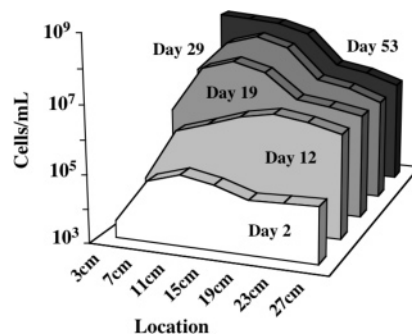


FIGURE 2. Spatiotemporal changes in the planktonic cell concentration of *D. vulgaris* during biostimulation. Locations represent distances along the direction of flow, with the lower values located near the inlet.

Solution samples taken along the multi-port column indicated that the location of active sulfate-reduction shifted downward (i.e., toward the inlet end) over time. Solute concentrations for a location 4.0 cm from the inlet end are shown in Figure 1B. The overall trend with time for the five species was similar for the two locations; however, the onset of change for each was delayed by 7–10 days, as was the rate of utilization. Neither lactate nor metal concentrations were completely depleted at the 4.0 cm location until day 22. This is in contrast to the 19.0 cm location (Figure 1A), where both species had reached sparing amounts by day 12.

The concentration of planktonic cells in the multi-port column exhibited a similar downward shift with time (Figure 2). Cell concentrations ranged from 10³ to 10⁵ cells/mL on day 2, with the highest concentrations near the point of inoculation. These values increased by nearly 2 orders of

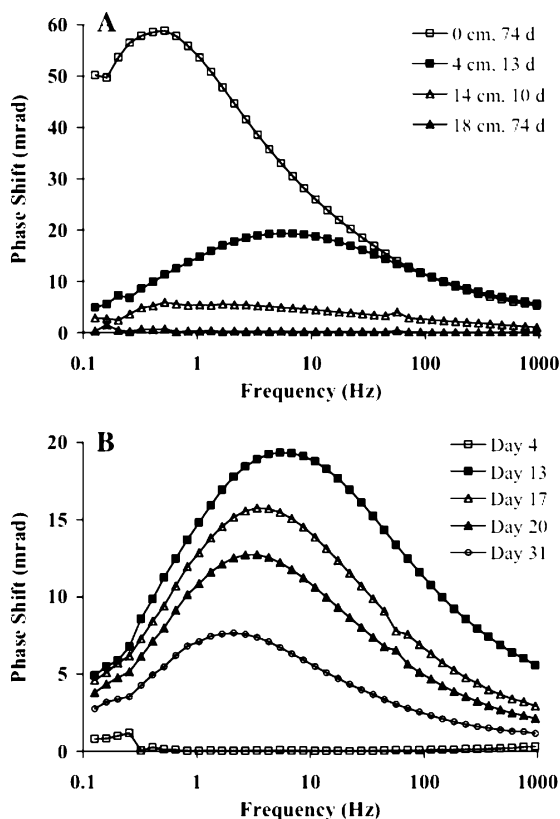


FIGURE 3. (A) Maximum phase shift relative to baseline for four locations, with each location measured starting from the base. The phase maxima occurred at different times for each location as shown. No anomaly was observed for the 18 cm location or for similar locations lacking significant mineralization. (B) Temporal development of the 4 cm phase anomaly.

magnitude by day 12, and the greatest increases were for the downgradient locations. From day 19 through the end of the experiment, the greatest increases in cell concentration occurred closer to the base, from 4 to 12 cm. Although downgradient concentrations decreased with time after day 19, they remained elevated by at least 2 orders of magnitude and appeared to reach a steady-state level. Although not shown in Figure 2, the cell concentration profiles for days 64 and 53 exhibited nearly identical trends.

Geophysical Response to Biomineralization. Complex Resistivity. Differences between the phase (ϕ) of the injected current and the resulting potential fields were used to identify regions exhibiting anomalous phase behavior. The maximum observed phase response at four column locations is shown in Figure 3A. Deviations began after 6 days near the point of inoculation (14 cm), reaching a maximum of 6 mrad on day 10. Larger anomalies of 20 mrad were observed after 13 days at a location 4 cm from the base, and both locations coincided with the visible accumulation of mineral precipitates (see Supporting Information). No significant deviations in ϕ were observed for sediments located between these two positions or for downgradient locations (18 cm), all of which lacked significant mineralization. Because no electrodes were located at the base, heavily mineralized sediments were removed from the bottom of the column (0 cm) after 74 days to better assess their phase response. These sediments exhibited the largest phase shifts, with values nearly 60 mrad above those of control sediments. No significant phase shifts were observed at similar locations along the length of the metal-amended abiotic control column.

The anomalous phase behavior observed 4 and 14 cm above the base exhibited a time-varying response, with values

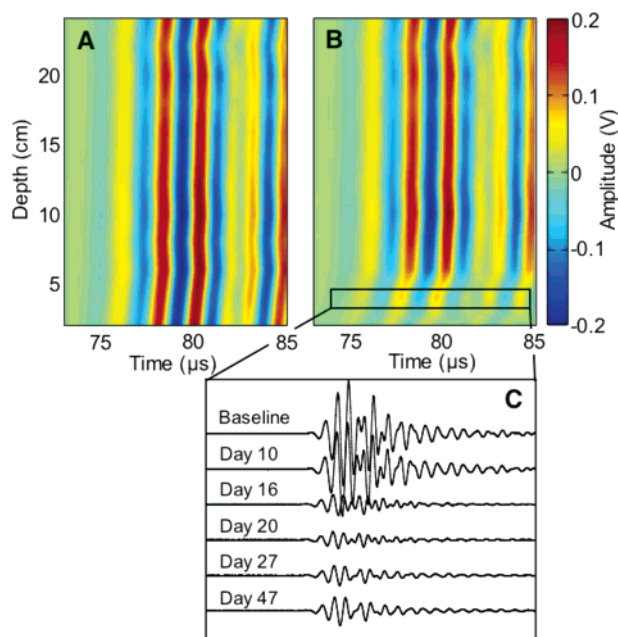


FIGURE 4. (A) Baseline acoustic waveforms associated with propagation through the center of the column. Both amplitude and velocity information can be extracted from the waveforms, with amplitudes plotted according to color and velocities related to the arrival time of the first color transition ($\sim 75 \mu$ s). (B) Identical slice taken after 20 days; flow direction is upward for both images with the influent end at the bottom. (C) Acoustic data illustrating variations in the waveform amplitude associated with the 2 cm sampling position.

of ϕ decreasing for both locations over time. The temporal variability in the phase response for the 4 cm location is shown in Figure 3B. Both the maximum phase shift and the frequency at which it occurred decreased with time, although a well-defined phase anomaly persisted for this location throughout the experimental period.

Acoustic Wave Propagation. The acoustic wave signatures began to deviate from their baseline values 10 days after biostimulation began. Signals became increasingly attenuated over time with only modest increases in wave velocity. Signal modifications were strongly localized within an area near the column base (Figure 4A,B). As compared to initial conditions, amplitudes decreased by 86 and 36% at locations 2 and 6 cm from the base, respectively, reaching minimum values 20 days into the experiment (Figure 4C). Sediment velocities increased by no more than 1 and 0.5% for the same locations. As with the phase responses, all changes tracked the accumulation of mineral precipitates. Only modest deviations in amplitude (less than or equal to $\pm 4\%$) were observed for the downgradient locations, with velocities never exceeding 0.4% of their baseline values. Identical measurements made on a control column over the same period showed little variability in either amplitude or velocity, deviating by no more than ± 2 or $\pm 0.3\%$, respectively.

The anomalous acoustic signals also exhibited a time-varying response, with wave amplitudes rebounding slightly from their most attenuated levels. The onset of the rebound occurred at different times for the locations that had exhibited amplitude decreases (2, 4, and 6 cm). By day 27, amplitudes had increased above their lowest levels by 11 and 16% for the 4 and 6 cm locations, respectively, and remained at these levels for the remainder of the test. Amplitudes for the 2 cm location did not rebound significantly until day 47, at which time they increased by 11% above their lowest level (Figure 4C). At no point did wave amplitudes in this region return to baseline levels.

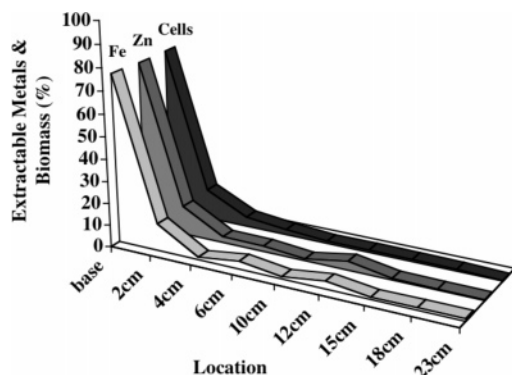


FIGURE 5. Total extractable Zn, Fe, and viable biomass (cells) as a function of distance from the influent end; flow direction was from base to the higher valued locations.

Hydraulic Conductivity. Variations in the saturated hydraulic conductivity (K_s) of the sediments were observed over the course of the experiment. Reductions in K_s for the inoculated column were modest over the first 17 days, decreasing by 12% from an initial value of 1.04×10^{-4} m/s. Another measurement made on day 20 showed no change in K_s over the 3 day interval. As the visible accumulation of mineral precipitates continued, the reduction in K_s became more pronounced. By day 53, the value of K_s reached 4×10^{-6} m/s, a total decrease of 96% from baseline. Measurements of K_s for the abiotic control sediments showed no significant deviation from baseline over the same time interval, with initial and final values of 8.5×10^{-5} and 8.2×10^{-5} m/s, respectively.

Microbe–Mineral Associations. Post-experimental analysis allowed us to correlate the observed changes in geophysical signals with the distribution of mineral precipitates and microbial biomass. Total extractable metal concentrations ranged from 99 to $0.5 \mu\text{mol/g}$ sediment for Zn and $128\text{--}0.1 \mu\text{mol/g}$ sediment for Fe. Metal enrichment was concentrated toward the base of the columns (Figure 5), with 76% of the extractable Zn and Fe recovered within the first 2 cm, corresponding to a volumetric enrichment of 1.4%. Minor enrichments of both Zn (18%) and Fe (17%) were recovered 2–6 cm from the inlet end, with an additional enrichment (~4%) recovered 12 cm from the end, near the initial point of inoculation. Viable biomass determined by phospholipid fatty acid analysis of grain-affixed cells varied from 1.6×10^9 to 3.3×10^6 cells/g sediment. The final cell concentrations along the columns paralleled those of the metals (Figure 5), with 96% of the biomass recovered within the first 6 cm. Unlike the metals, no minor enrichments in biomass were found at locations downgradient from 6 cm. The recovered lipid biomarkers, in particular, the branched lipids i17:1 ω 9c and 18:1 ω 7c, were consistent with those previously reported for the genus *Desulfovibrio* (23). The uniformity in the type of extractable lipids was indicative of a monoculture, suggesting that little or no contamination occurred over the experimental period.

Scanning and transmission electron microscopy documented significant spatial variability in the abundance and distribution of cells and their associated mineral products. SEM analysis of basal sediments revealed grain coatings consisting of dense accumulations of sulfide-encrusted microbes. These coatings frequently extended into pores, spanned adjacent grains, and occluded pore throat openings (Figure 6A). SEM analysis of chemically unfixed samples revealed cohesive metal sulfide aggregates that adopted the shape of the underlying cells (Figure 6B,C). The material deposited within the cells was spatially persistent, maintaining its shape even after cell death (Figure 6C).

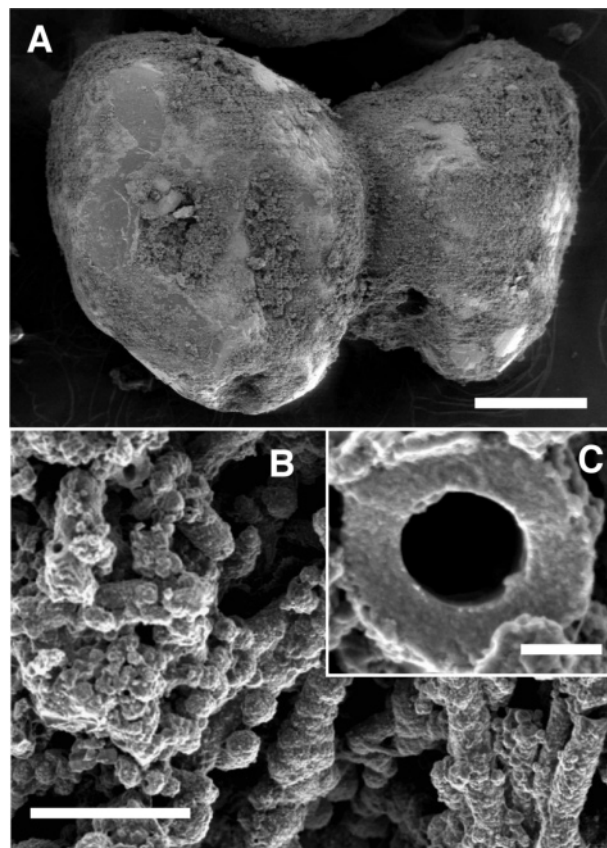


FIGURE 6. (A) SEM image of encrusted quartz grains from the column base; precipitates spanned multiple grains obstructing pore throat openings. Bar: $200 \mu\text{m}$. (B) SEM image of metal sulfide encrusted microbes and spherical aggregates. Bar: $10 \mu\text{m}$. (C) High-resolution SEM image of a fractured cell encrusted in compositionally mixed ZnS and FeS. Bar: $0.5 \mu\text{m}$.

TEM-based analysis of the precipitates revealed them to be a mixture of sphalerite (ZnS) and mackinawite (FeS), with an average crystal size of 3 nm. Mineralogical identification was accomplished through analysis of the selected area electron diffraction patterns (data not shown), with elemental compositions confirmed using energy-dispersive X-ray spectroscopy. Aggregates frequently spanned the outer membrane of cells (Figure 7A), occasionally filling, and in some cases swelling, the periplasmic space. Aggregates of ZnS and FeS ranged from clusters of nanocrystals to larger assemblages up to $10\text{--}20 \mu\text{m}$ in diameter (Figure 7B,C).

The number of precipitate-free cells increased with distance from the influent end (4–6 cm). Cells in these regions formed biofilms that coated mineral precipitates (Figure 8A,B) that were morphologically and compositionally distinct from those found closer to the influent end. The dominant mineral was FeS with a platy crystal habit (Figure 8C), which appeared to be spatially continuous across grain surfaces (Figure 8A). The FeS laths may have resulted from the aging of a few nanometer diameter particles that formed early in the experiment near the initial point of inoculation (Figure 7C).

SEM analysis of the low biomass sediments from non-mineralized portions of the columns revealed significant variability from those sediments recovered within the first few centimeters of flow (see Supporting Information). No evidence of biomineralization was detected, nor were the cells found within biofilms; rather, the observed cells were found to be planktonic and free of membrane-bound mineralization. Sediments from the downgradient locations closely resembled those recovered from the noninoculated

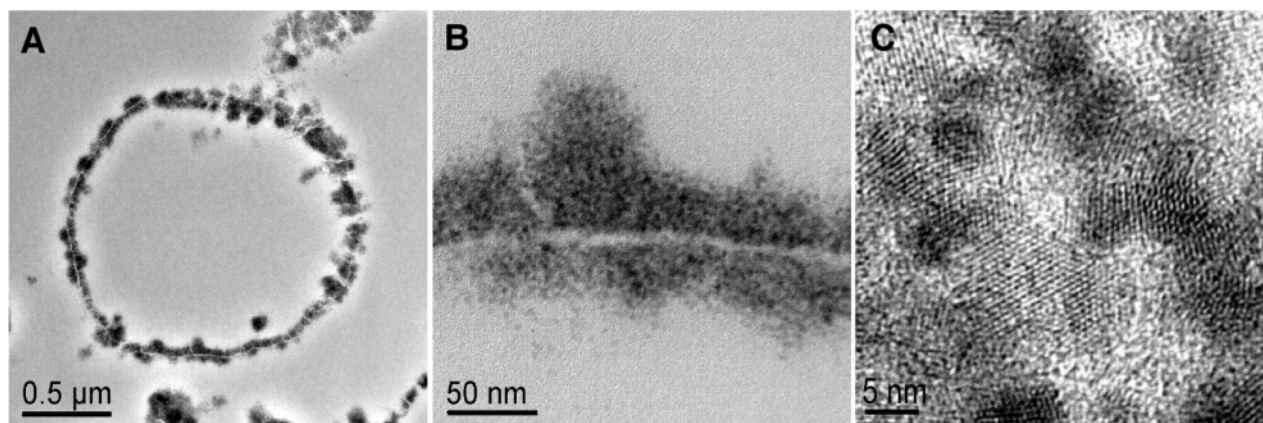


FIGURE 7. (A and B) Cross-sectional TEM images of a single *D. vulgaris* cell with membrane-bound ZnS and FeS precipitates. (C) High-resolution TEM revealed the nanocrystalline character of the precipitates with a typical particle size of 3–5 nm.

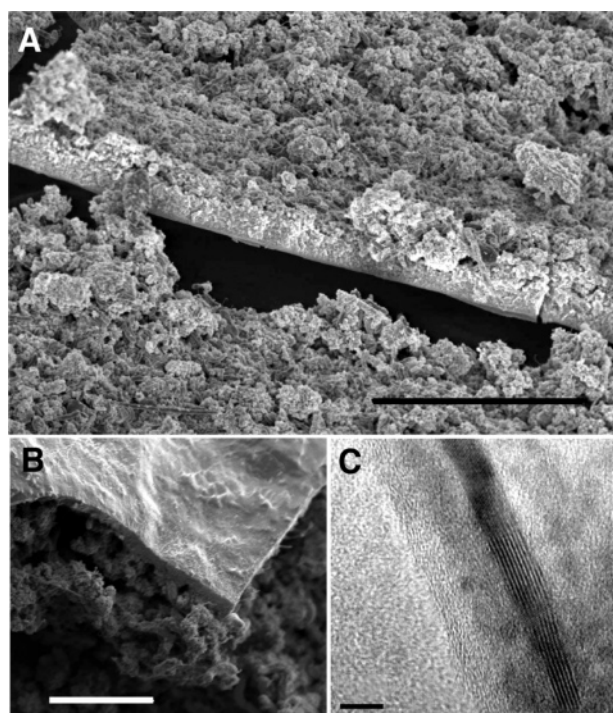


FIGURE 8. (A) SEM image of a grain surface located 4 cm from the column base showing biofilm development atop dense accumulations of mineral precipitates. Bar: 20 μm . (B) SEM image of a similar location showing nonencrusted cells screening compacted sulfide precipitates. Bar: 5 μm . (C) High-resolution TEM image of coarsened, aged sulfides from the same location. Bar: 5 nm.

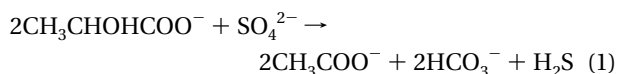
controls, with little alteration of grain surfaces and no obstruction of pore throats.

Discussion

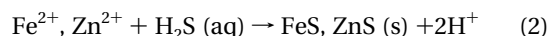
The results presented in this study illustrate the complex phenomena that occur even under relatively controlled column conditions and illustrate the utility of geophysical methods for monitoring the pore scale changes associated with the stimulation of sulfate-reducing bacteria and the immobilization of aqueous metals. The role of sulfate-reducing bacteria in the precipitation of toxic metals is well-documented, and strategies involving their stimulation are under investigation for the field scale remediation of contaminated sites (24, 25). Our results show that initial variations in both complex resistivity and acoustic wave signatures correlate well with biogeochemical measurements indicative of sulfate reduction and that they are related to

the nucleation and accumulation of metal sulfide precipitates within the pore space. In addition, time-varying changes in the geophysical signals appear to offer insight into the aggregation state of the sulfides and may be indicative of crystal growth and aging.

Temporal changes in the effluent concentration of lactate, acetate, and sulfate (Figure 1A,B) correspond to the onset (after 3–5 days) and pseudo-steady-state maintenance of microbial sulfate reduction (5–73 days). Stoichiometric amounts of acetate were produced with lactate consumed, suggesting that the primary organic carbon-consuming reaction is the incomplete oxidation of lactate to acetate and CO_2 , an observation consistent with that of other workers (26). Aqueous concentrations of both Zn and Fe were observed to decrease in direct proportion to decreasing sulfate concentrations. As such, the stimulation of *D. vulgaris* by lactate amendment and the resulting sequestration of metals in insoluble sulfides can be expressed as a two-step process:



The aqueous hydrogen sulfide may then react with any metals in solution (e.g., Zn^{2+} , Fe^{2+}) precipitating as metal sulfides



Given the low solubility products (K_{sp}) of most metal sulfides (e.g., K_{sp} values ranging from $10^{-17.2}$ for FeS to $10^{-25.2}$ for ZnS), even low concentrations of hydrogen sulfide can effectively remove aqueous metals from solution (27, 28).

Because of the low solubility of the sulfides and the rapid rate of precipitation (29), the formation and accumulation of ZnS and FeS was largely confined to the region of active sulfate reduction. The spatiotemporal changes in both solute and planktonic cell concentrations (Figures 1B and 2) suggested chemotaxis by *D. vulgaris* toward the region of greatest substrate concentration (30). Although the direction of chemotaxis was against flow, the specific flux near the grain boundaries was sufficiently low to allow for easy motility. As feed solutions were introduced at the bottom of each column, substrate concentrations were always highest in this area. The start of the experiment, however, coincided with the greatest cell concentration near the point of inoculation (Figure 2, day 2). As a result, microbial sulfate reduction began in this region (14 cm, measured from the column base), as did the initial accumulation of sulfide precipitates. By day 19, the distribution of cells in the columns had reached stable levels (Figure 2), with concentrations near the inlet 2 orders of magnitude higher than those down-

gradient. The eventual migration of cells toward the inlet end did not necessarily proceed in a linear fashion, as cells were already present at low concentrations (10^3 cell/mL) in this area on day 2. Given the nature of exponential growth and their proximity to elevated substrate concentrations, cells in the first 2–4 cm may have rapidly overtaken the initially larger downgradient cell populations. Once cell growth in this region outpaced the available supply of nutrients, the reduction of sufficient sulfate to remove all subsequent metals from solution (~ 0.67 mM) was occurring within the first few centimeters of flow. Such an effect can be observed in the differing rates of substrate utilization for two locations (Figure 1), with the location exhibiting a more rapid rate of utilization (19.0 cm) corresponding to the region of initially higher cell concentration.

The distribution of extractable metals and viable biomass after 78 days reflects such a sequence of events, with enrichment heavily concentrated toward the base. In a similar fashion, the temporal geophysical anomalies correlated directly with the formation and accumulation of mineral precipitates (Figure 3A). The initial phase shifts in the complex resistivity data were concomitant with the early-stage removal of metals from solution (day 6), both of which occurred near the point of inoculation. Subsequent phase shifts, however, did not progressively trend toward the inlet end. Rather, they shifted location abruptly, and by day 13, the largest phase shifts were associated with sediments closer to the point of nutrient influx. Perhaps due to their lower sensitivity to mineral precipitates, acoustic waves were not significantly attenuated until day 16 once larger sulfide enrichments had occurred, and then only in first 6 cm of flow (Figure 4C). The shift in sulfate reduction toward the column base caused metal sequestration to be confined to this region, and downgradient sediments experienced few of the physiochemical changes that resulted in time-varying geophysical signatures. As a result, basal sediments exhibited the most significant deviations in both phase response and acoustic wave amplitude, while no significant signal changes were observed for either unmineralized or sparingly mineralized regions of the column.

The properties of the nanocrystalline precipitates and their nucleation and growth within the pore space are critical in interpreting the geophysical responses. As a result of the numerous unsatisfied bonds along their surfaces, individual metal sulfide nanocrystals are expected to have both high surface area and charge density. Freshly precipitated ZnS and FeS are therefore expected to modify the electrical charge transport through the sediments by encouraging a flow of dissolved ions to and from the metal–electrolyte interface. The resulting ionic concentration gradients will oppose ionic migration under an applied electric field, leading to the anomalous phase behavior observed during the complex resistivity measurements. As evident from the phase response, this polarization is further enhanced when minor concentrations of redox active ions in solution (e.g., HS^- resulting from dissociation of H_2S) engage in reversible electrochemical reactions at metal sulfide surfaces (eq 2) (31). Such effects are well-documented for metal-rich ore deposits (32) and form the basis for using low-frequency electrical methods in mineral prospecting (33).

The decreases in acoustic wave amplitude are attributed to the development of differential elastic moduli resulting from the accumulation of metal sulfide-encrusted microbes within the pore space. The sulfide aggregates are themselves a distinct porous material embedded within the main pores of the quartz sand (Figures 4B,C and 5B). As such, when an acoustic wave compresses the entire sand/sulfide assemblage, the micropores of the aggregates respond with a different fluid pressure than the macropores of the sand grains. This difference in fluid pressure results in a viscous

flow of fluid from the aggregates to the main pores that attenuates acoustic energy. Such an effect can account for large decreases in amplitude and can be modeled using recently developed double-porosity models of acoustic wave attenuation (17). The models indicate that the attenuation mechanism operates over a wide range of frequencies and imply the applicability of our high-frequency laboratory measurements (1000 kHz) to those made under field conditions (0.1–1 kHz). Differences between the elastic moduli of the sulfide bearing pores and those not containing appreciable precipitates may have further enhanced this attenuation mechanism.

Several possible factors likely contributed to the time-varying nature of the geophysical signatures that followed sulfide precipitation. Temporal decreases in the phase response may have been the result of two dynamic effects. First, biofilm polymers may have screened early-formed sulfides from the pore fluids, diminishing the surface effect of the sulfides on electrolytic charge migration and electrochemical reactivity (Figure 8A,B). In addition, the growth and aging of FeS precipitates (Figure 8C) may have led to the formation of electrically conductive short-circuits along grain surfaces that diminished the phase response (34). The development of such features would be expected to increase the bulk electrical conductivity of the sediments over time, and such an effect was observed (see Supporting Information). Temporal variability in the phase response for the 4 cm location (Figure 3B) was accompanied by an inverse change in the measured bulk conductivity of the sediments, a value controlled by the relative ease with which current-carrying ions migrate through the pore fluid and along grain surfaces. As the measurement of influent conductivities showed little variation over the experiment, the increase in bulk conductivity is inferred to be the result of an increase in the charge-carrying capacity of conductive grain-coatings (e.g., FeS). This interpretation is supported by published values of the conductivity of both poorly crystalline and bulk FeS mineral phases, with the conductivity of amorphous $\text{FeS}_{1.5}$ found to be 5.4×10^{-6} S/m (35) and that of the bulk form found to be $\sim 10^4$ S/m (14). The decrease in the frequency of the maximum phase shift with time also suggests precipitate growth and aging (Figure 3B); experiments performed on mixtures of sand and metal sulfides have found a similar inverse correlation between sulfide grain size and frequency (32, 36). On the basis of the available data, we might expect a decrease in critical frequency of several orders of magnitude as the individual nanocrystals aggregate; our data exhibit a similar trend over time, with frequencies decreasing by nearly 1 order of magnitude.

The rebound in acoustic wave amplitudes may have resulted from a combination of factors. These include increasing homogeneity in the distribution of mineral precipitates within the pores as time elapsed and the loss of secondary porosity structures brought about by the coarsening of the metal sulfides. In addition, researchers have found large variations in elastic moduli between nanoparticulate and bulk phases of the same material. Pan et al. (37) have shown the nanocrystalline form of ZnS to have significantly higher bulk modulus than its bulk counterpart. As a result, the contrast in the elastic moduli between mineralized and nonmineralized regions decreased as growth and aging proceeded, leading to a slightly diminished attenuation mechanism.

Coarsening of the nanoparticulate sulfide phases is most likely controlled by growth through oriented attachment, which involves the spontaneous reorganization of neighboring nanoparticles (Figure 7C) such that they share a common crystallographic axis (38). Crystal growth proceeds as the two particles join along a planar interface, and the process is repeated along the new terminating ends (Figure 8C). The

particle movement needed to achieve orientation within the random aggregates may have arisen through a combination of Brownian motion within the saturated pores and shear forces resulting from fluid flow through the porous medium. The later contribution would be enhanced as pore fluid velocities increased due to pore throat restrictions resulting from the accumulation of precipitates and biomass (Figure 6A). Given the observed 96% decrease in saturated hydraulic conductivity, numerous such restrictions were likely.

In cases where remediation of aqueous metals is accomplished through precipitation of insoluble phases, such a growth mechanism is highly desirable (5). Any increase in the overall size of the precipitates as a result of crystallographic growth typically acts to decrease their mobility and should increase their likelihood of sequestration within the pore space (39, 40). Our results suggest that geophysical monitoring may offer insight into the time-varying aggregation state of the sulfides. The variations in the phase response of the complex resistivity data correlate well with the initially nanoparticulate form of the sulfides (Figure 7B,C). Their large specific surface area and discontinuous nature induce measurable phase anomalies. As individual nanocrystals aggregate into larger clusters around cell surfaces, growth through oriented attachment proceeds. This results in an overall decrease in the phase response as mineral coarsening and growth leads to the formation of continuous crystals that span multiple grains. Similarly, as growth proceeds and the aggregates become more densely packed (Figure 8B), the secondary porosity structure that led to the early-stage attenuation of acoustic waves is diminished, resulting in a slight rebound in amplitudes.

Here, we have shown that the stimulation of sulfate-reducing microorganisms and the associated formation of insoluble metal sulfides create physical property changes that are directly detectable using geophysical techniques. We have resolved spatiotemporal changes in complex resistivity and acoustic wave propagation resulting from variations in the electric charge carrying capacity and elastic moduli of precipitates and pore fluids. The changes persisted over time and were confined exclusively to those regions where metals were sequestered in insoluble precipitates. Temporal changes in the geophysical signals appear to offer insight into the aggregation state of the sulfides and may be indicative of pore scale crystal growth and aging, with such a result having implications for the fate and transport of the microbe-induced precipitates. Our laboratory results are relevant to the larger spatial scales of the natural environment where methods currently used for field-scale geophysical monitoring may be used in an analogous fashion. These results show the potential of using complex resistivity and acoustic wave techniques for remotely monitoring regions of contaminant sequestration via biomineralization and for evaluating the overall long-term stability of such precipitates.

Acknowledgments

Funding for this study was provided by the Environmental Management Science Program, Office of Biological and Environmental Research, U.S. Department of Energy (DOE) (Grant DE-AC03-76SF00098). Electron microscopy was carried out in the Environmental Molecular Sciences Laboratory, a national scientific user facility sponsored by DOE's Office of Biological and Environmental Research and located at Pacific Northwest National Laboratory. We thank Jim Young for his assistance in preparing and analyzing the SEM samples and Sharon Borglin (LBNL) for her help with the PLFA analysis.

Supporting Information Available

Four figures are available to help in the visualization of the column design and the products of biomineralization, as

well as additional time-varying complex resistivity data that support the hypothesis of mineral coarsening. This material is available free of charge via the Internet at <http://pubs.acs.org>.

Literature Cited

- (1) Ehrlich, H. L. Microbes as geologic agents: Their role in mineral formation. *Geomicrobiol. J.* **1999**, *16*, 135.
- (2) Drury, W. J. Treatment of acid mine drainage with anaerobic solid-substrate reactors. *Water Environ. Res.* **1999**, *71*, 1244.
- (3) Schultze-Lam, S.; Fortin, D.; Davis, B. S.; Beveridge, T. J. Mineralization of bacterial surfaces. *Chem. Geol.* **1996**, *132*, 171.
- (4) Rittler, K. A.; Drever, J. I.; Colberg, P. J. S. Precipitation of arsenic during bacterial sulfate reduction. *Geomicrobiol. J.* **1995**, *13*, 1.
- (5) Anderson, R. T.; Vrionis, H. A.; Ortiz-Bernad, I.; Resch, C. T.; Long, P. E.; Dayvault, R.; Karp, K.; Marutzky, S.; Metzler, D. R.; Peacock, A.; White, D. C.; Lowe, M.; Lovley, D. R. Stimulating the in situ activity of geobacter species to remove uranium from the groundwater of a uranium-contaminated aquifer. *Appl. Environ. Microbiol.* **2003**, *69*, 5884.
- (6) Chapelle, F. H. The significance of microbial processes in hydrogeology and geochemistry. *Hydrogeol. J.* **2000**, *8*, 41.
- (7) Suzuki, Y.; Kelly, S. D.; Kemner, K. M.; Banfield, J. F. Radionuclide contamination—nanometer-size products of uranium bioreduction. *Nature* **2002**, *419*, 134.
- (8) Rubin, Y.; Hubbard, S. S. *Hydrogeophysics*; Springer: Berlin, 2005.
- (9) Kemna, A.; Binley, A.; Slater, L. Crosshole IP imaging for engineering and environmental applications. *Geophysics* **2004**, *69*, 97.
- (10) Geller, J. T.; Kowalsky, M. B.; Seifert, P. K.; Nihei, K. T. Acoustic detection of immiscible liquids in sand. *Geophys. Res. Lett.* **2000**, *27*, 417.
- (11) Slater, L. D.; Lesmes, D. IP interpretation in environmental investigations. *Geophysics* **2002**, *67*, 77.
- (12) Atekwana, E. A., Jr.; D. D. W.; Duris, J. W.; Rossbach, S.; Atekwana, E. A.; Sauck, W. A.; Cassidy, D. P.; Means, J.; Legall, F. D. In situ apparent conductivity measurements and microbial population distribution at a hydrocarbon-contaminated site. *Geophysics* **2004**, *69*, 56.
- (13) Abdel Aal, G. Z.; Atekwana, E. A.; Slater, L. D.; Atekwana, E. A. Effects of microbial processes on electrolytic and interfacial electrical properties of unconsolidated sediments. *Geophys. Res. Lett.* **2004**, *31*, L12505.
- (14) Telford, W. M.; Geldart, L. P.; Sheriff, R. E. *Applied geophysics*; Cambridge University Press: New York, 1998.
- (15) Slater, L. D.; Glaser, D. R. Controls on induced polarization in sandy unconsolidated sediments and application to aquifer characterization. *Geophysics* **2003**, *68*, 1547.
- (16) Li, X.; Pyrak-Nolte, L. J. Acoustic monitoring of sediment-pore fluid interaction. *Geophys. Res. Lett.* **1998**, *25*, 3899.
- (17) Pride, S. R.; Berryman, J. G.; Harris, J. M. Seismic attenuation due to wave-induced flow. *J. Geophys. Res.* **2004**, *109*, 1.
- (18) Widdel, F.; Bak, F. *The prokaryotes*; Springer-Verlag: Berlin, 1991.
- (19) Levin, M. A.; Seidler, R. J.; Rogul, M. *Microbial ecology: Principles, methods, and applications*; McGraw-Hill: New York, 1992.
- (20) Ulrich, C.; Slater, L. D. Induced polarization measurements on unsaturated, unconsolidated sands. *Geophysics* **2004**, *69*, 762.
- (21) White, D. C.; Ringelberger, D. B. *Techniques in microbial ecology*; Oxford University Press: New York, 1998.
- (22) Vandevivere, P.; Baveye, P. Sampling method for the observation of microorganisms in unconsolidated porous-media via scanning electron microscopy. *Soil Sci.* **1992**, *153*, 482.
- (23) Kohring, L. L.; Ringelberg, D. B.; Devereux, R.; Stahl, D. A.; Mittelman, M. W.; White, D. C. Comparison of phylogenetic relationships based on phospholipid fatty-acid profiles and ribosomal-rRNA sequence similarities among dissimilatory sulfate-reducing bacteria. *FEMS Microbiol. Lett.* **1994**, *119*, 303.
- (24) White, C.; Gadd, G. M. Mixed sulphate-reducing bacterial cultures for bioprecipitation of toxic metals: Factorial and response-surface analysis of the effects of dilution rate, sulphate, and substrate concentration. *Microbiology* **1996**, *142*, 2197.
- (25) Smith, W. L.; Gadd, G. M. Reduction and precipitation of chromate by mixed culture sulphate-reducing bacterial biofilms. *J. Appl. Microbiol.* **2000**, *88*, 983.
- (26) Voordouw, G. Carbon monoxide cycling by *Desulfovibrio vulgaris* hildenborough. *J. Bacteriol.* **2002**, *184*, 5903.

- (27) Drzyzga, O.; El Mamouni, R.; Agathos, S. N.; Gottschal, J. C. Dehalogenation of chlorinated ethenes and immobilization of nickel in anaerobic sediment columns under sulfidogenic conditions. *Environ. Sci. Technol.* **2002**, *36*, 2630.
- (28) Ingvorsen, K.; Jorgensen, B. B. Kinetics of sulfate uptake by freshwater and marine species of *Desulfovibrio*. *Arch. Microbiol.* **1984**, *139*, 61.
- (29) Poulson, S. R.; Colberg, P. J. S.; Drever, J. I. Toxicity of heavy metals (Ni, Zn) to *Desulfovibrio desulfuricans*. *Geomicrobiol. J.* **1997**, *14*, 41.
- (30) Johnson, M. S.; Zhulin, I. G.; Gapuzan, M. E. R.; Taylor, B. L. Oxygen-dependent growth of the obligate anaerobe *Desulfovibrio vulgaris* hildenborough. *J. Bacteriol.* **1997**, *179*, 5598.
- (31) Angoran, Y.; Madden, T. R. Induced polarization: A preliminary study of its chemical basis. *Geophysics* **1977**, *42*, 788.
- (32) Wong, J. An electrochemical model of the induced-polarization phenomenon in disseminated sulfide ores. *Geophysics* **1979**, *44*, 1245.
- (33) Pelton, W. H.; Ward, S. H.; Hallof, P. G.; Sill, W. R.; Nelson, P. H. Mineral discrimination and removal of inductive coupling with multifrequency-IP. *Geophysics* **1978**, *43*, 588.
- (34) Vinegar, H. J.; Waxman, M. H. Induced polarization of shaly sands. *Geophysics* **1984**, *49*, 1267.
- (35) Li, J.; Nazar, L. F. Mesosstructured iron sulfides. *Chem. Commun.* **2000**, *18*, 1749.
- (36) DeWitt, G. W. Parametric studies of induced polarization spectra, Ph.D. Thesis, University of Utah, Salt Lake City, UT, 1979.
- (37) Pan, Y. W.; Qu, S. C.; Dong, S. S.; Cui, Q. L.; Zhang, W. W.; Liu, X. Z.; Liu, J.; Liu, B. B.; Gao, C. X.; Zou, G. T. An investigation on the pressure-induced phase transition of nanocrystalline ZnS. *J. Phys.: Condens. Matter* **2002**, *14*, 10487.
- (38) Penn, R. L.; Banfield, J. F. Imperfect oriented attachment: Dislocation generation in defect-free nanocrystals. *Science* **1998**, *281*, 969.
- (39) Loveland, J. P.; Bhattacharjee, S.; Ryan, J. N.; Elimelech, M. Colloid transport in a geochemically heterogeneous porous medium: Aquifer tank experiment and modeling. *J. Contam. Hydrol.* **2003**, *65*, 161.
- (40) Ryan, J. N.; Elimelech, M. Colloid mobilization and transport in groundwater. *Colloids Surf., A* **1996**, *107*, 1.

Received for review February 25, 2005. Revised manuscript received June 24, 2005. Accepted July 12, 2005.

ES0504035